# Microstructural changes induced by Er and Zr additions to A356 alloy investigated by thermal analyses and STEM observations

M. Colombo, M. Albu, E. Gariboldi, F. Hofer

**Abstract:**
This work is aimed at characterizing the changes induced in the microstructure of an Al-7Si-0.4Mg (A356) alloy when different amounts of Er and Zr are added. The addition of E and Zr caused the precipitation of $Al_3Er$ and $Al_3$(Er, Zr) dispersoids during solution heat treatment, as it was shown by isothermal DSC tests performed at the solution treatment temperature, microhardness measurements on samples subjected to different solution treatment time and STEM micrographs. The age hardening response of Er- and Zr-containing A356 is improved, thanks to the formation of further $Al_3Er$ and $Al_3$(Er, Zr) dispersoids during aging. Er- and Zr-containing particles were also identified inside eutectic Si and were identified as $Al_2Si_2Er$ and $Al_2Si_2$(Er, Zr) for E3 and EZ35, respectively. Finally, an Er-rich layer was identified at the interface between eutectic Si and Al after thermal treatment, possibly formed by Er atoms diffusing along the Si twins and accumulating at the eutectic Si interface with the Al matrix.

**Introduction:**
A356 (Al7Si0.4Mg) cast alloy is widely used in several industrial fields, especially where high specific mechanical properties and excellent castability are required [1].
Its good mechanical properties derive from its significant age hardening response when subjected to a proper heat treatment [2-5]. The precipitation sequence and phase evolution during aging of Al-Si-Mg cast alloys have been recently described as those of excess Si Al-Mg-Si wrought alloys [6]:

Al SSS → Mg/Si co-clusters (GP-zones) → β'' → β' + Si → β + Si

Where SSS stands for supersaturated solid solution and GP for Guinier-Preston zone.
A recent literature study demonstrated that, in the peak aged condition, the main strengthening dispersoids in A356 are β" needles [6]. As aging proceeds, the dispersoids evolve, progressively enriching in Mg [7], lose coherency with the matrix and coarsen. The natural consequence of the last two phenomena is the reduced pinning ability of the dispersoids for dislocations, which implies the degradation in mechanical properties typical of overaging.
The addition of rare earths and transition metals in the chemical composition of Al-Si-Mg alloys has proven to strengthen the material, thanks to the formation of additional dispersoids in intra-dendritic regions [8-10]. Specifically, some elements were found to form strengthening particles at temperatures comparable to those used during solution heat treatment of Al alloys [11, 12]. In this respect, in the last years, several researches were focused on the effects of combined additions of Er and Zr in pure Al [13-17]. These elements can lead to the formation of core-shell $Al_3$(Er, Zr) $L1_2$ dispersoids, that are coherent with the matrix up to a critical size and resistant to coarsening, maximizing the strengthening contribution [13-17].
Despite the positive action of Er and Zr on pure Al, there is still lack of a comprehensive characterization of the effects of combined additions of those elements to commercial Al-Si-Mg alloys.
Scope of this work is to study the influence of Er and Zr additions on the evolution of microstructural constituents, such as strengthening particles, during thermal treatment of a commercial Al7Si0.4Mg

alloy (A356), by means of Differential Scanning Calorimetry (DSC), microhardness tests and microstructural characterization with Scanning Transmission Electron Microscope (STEM).

## 2. Materials and Methods:

Al-15 wt. % Er and Al-10 wt. % Zr master alloys were added to a commercial A356 alloy, which was used as a reference, to obtain the chemical composition reported in Table 1.

**Table. 1:** Chemical composition (in wt. %) of the alloys used in this work, measured by GDOES analyses.

| | Si | Mg | Fe | Ti | B | Er | Zr | Al |
|---|---|---|---|---|---|---|---|---|
| **A356** | 7.02 | 0.41 | 0.07 | 0.14 | 0.0001 | - | - | bal |
| **E3** | 7.38 | 0.36 | 0.08 | 0.14 | 0.0001 | 0.28 | - | bal |
| **EZ35** | 6.85 | 0.34 | 0.09 | 0.12 | 0.0003 | 0.25 | 0.59 | bal |

Reference and master alloys were cast in an induction furnace at the casting temperature of 800 °C; the molten alloys were subjected to magnetic stirring, in order to minimize compositional inhomogeneities, and protected from oxidation with an Ar flux. The alloys were then poured in a stainless steel mould, preheated to 200 °C.

Samples extracted from similar positions of the cast bars were subjected to solution heat treatment (SHT) for different times up to 5 hours and cooled to room temperature by water quenching, to study the effect of the solubilization time on the microstructures of the alloys.

A further set of samples was subjected to SHT for 5 h, water quenched and subsequently aged at 200 °C up to 168 h. To minimize precipitation before the starting of aging, the quenched specimens were stored at -20 °C, for a maximum time of 30 minutes.

Microhardness tests were performed with an indenter load of 2.94 N and an indentation time of 15s on samples subjected to different SHT and aging times, to characterize the microstructural response of the alloys to high temperature exposure. Statistic relevance is guaranteed by 10 repetitions for each measurement condition. Aging response of the alloys was monitored by microhardness tests at different aging times.

Isothermal Differential Scanning Calorimetry (DSC) tests were carried out using a Setaram Labsys TGA/DTA-DSC equipment on samples in the as-cast state. Tests were performed in controlled atmosphere, with Ar fluxing in the furnace, on samples extracted from similar positions of the ingots and having a mass of 50 mg. The set thermal cycle is composed by a heating stage, from 20 °C to 520 °C with a heating rate of 30 °C/min and from 520 to 540 °C with a heating rate of 5 °C/min, by 5h hold at 540°C and finally cooling at RT at 30°C/min .

A selected set of specimens, identified for STEM analyses, were prepared by electro polishing and Ar ion-milling, with the help of a Precision Ion Polishing System (PIPS, Gatan Inc.) at a voltage of 4 kV. The incident angles of the ion cannons were set at 6° and 4° until perforation of the sample. STEM investigations were performed using a probe corrected FEI Titan G2 60–300 STEM microscope, with an X-FEG Schottky field-emission electron source operated at 300 kV (current of 150 pA, beam diameter of 1 Å). The microscope is also equipped with a FEI Super-X detector (Chemi-STEM technology), consisting of four separate silicon drift detectors and a Dual EELS - Gatan Imaging Filter (GIF) Quantum. High Angular Annular Dark Field (HAADF) and Annular Dark Field (ADF) detectors were used to acquire micrographs.

Samples were oriented along the $<1\ 0\ 0>_{Al}$ crystallographic direction, for better analysis of the nanometric dispersoids.

## 3. Results

### *3.1. Microhardness tests*

Microhardness evolution after SHT of different durations is reported in figure 1. Standard deviation for each alloy and SHT time is reported as error bars.

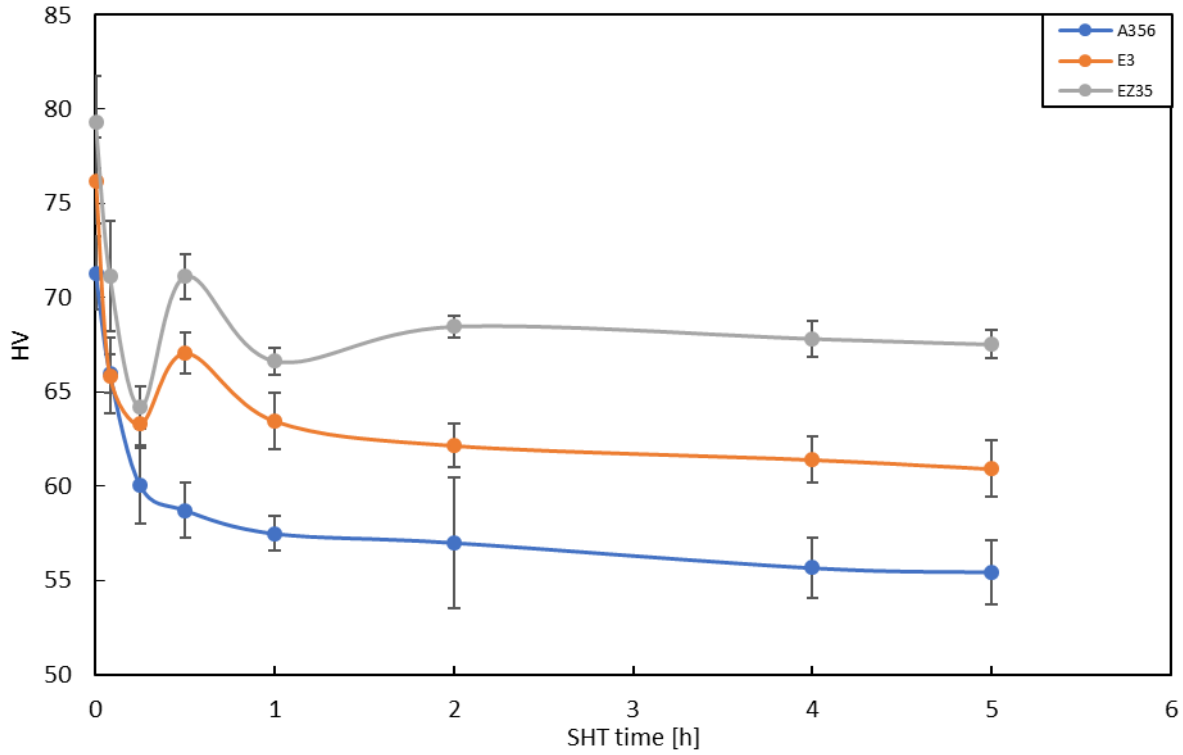


**Figure 1:** Microhardness of the investigated alloys of samples SHT for different times.

In the as-cast state the hardness of the alloys has a value of 71.3 HV, 76.2 HV and 79.3 HV for A356, E3 and EZ35, respectively.

The microhardness of A356 is shown to monotonically decrease as SHT duration increases, reaching an almost constant value after 2 h. The microhardness of the alloy E3 initially decreases, then shows a maximum at around 0.5 h and then decreases again. Finally, the microhardness of the alloy EZ35 initially decreases, then at 0.5 h shows a maximum and then, after a small drop, increases again, reaching an almost constant value after 2 h. After 5 h SHT A356 shows a microhardness value of 55.4 HV, while E3 and EZ35 are characterized by a microhardness of 60.9 HV and 66.7 HV, respectively, with an increase of 9.9% and 20.4% with respect to the reference alloy.

The aging response at 200 °C after 5 h SHT at 540 °C is reported in figure 2 for the three alloys.

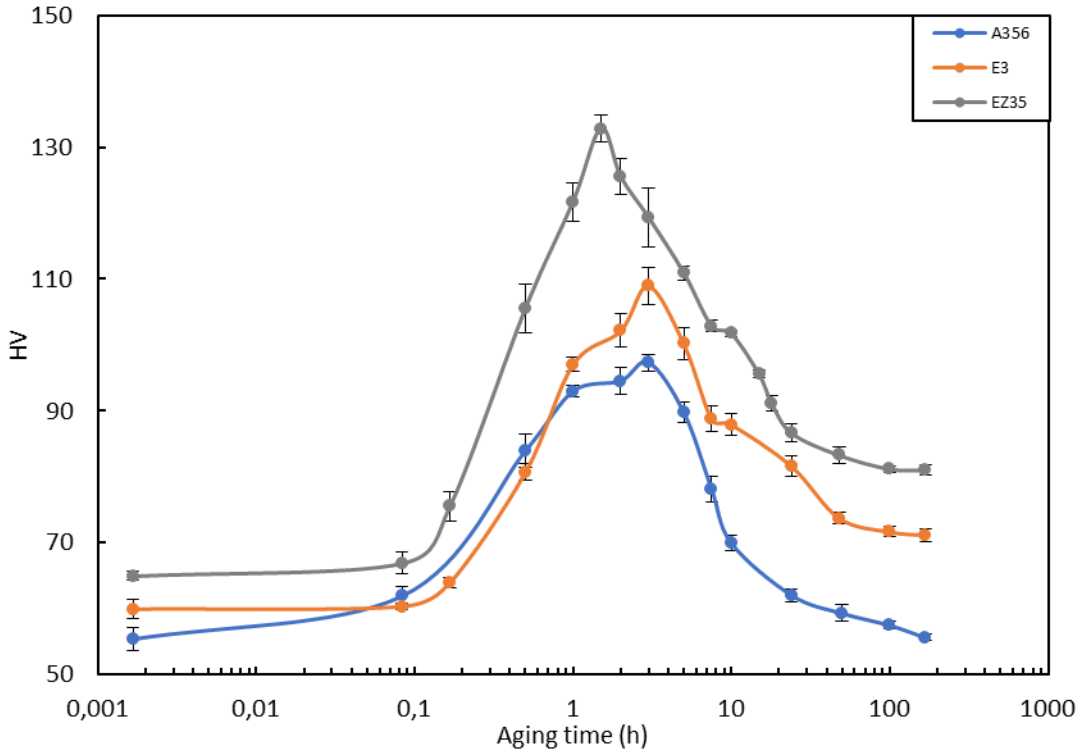


**Figure 2:** Aging response at 200 °C of the studied alloys after 5 h SHT.

The microhardness profile for short aging times show a rapid increase for all the alloys followed, in A356 and E3, by a reduced hardening response between 1 and 2 h and a subsequent steep increase up to the peak value, which is reached after 3 h. The maximum microhardness is 97.3 HV and 109.0 HV for A356 and E3, respectively, with an increase of 11.5%. The microhardness profile for EZ35, on the other hand, shows a monotonic increase up to the peak value, that is reached after 1.5 h. The maximum microhardness for EZ35 has a value of 132.8 HV, which is 21.8% and 36.5% higher than the value of E3 and A356, respectively.
For longer aging times the microhardness of the alloys decreases. Specifically, after 168 h aging A356 shows a microhardness value close to the one in the as-quenched condition, while E3 and EZ35 show a microhardness value of 71.1 and 81.0 HV, respectively, with an average increase of 28% and 45.7% with respect to the value of A356.

*3.2. Thermal analyses simulating SHT*

Alloys in the as-cast state are subjected to isothermal DSC tests, to simulate microstructural evolution during high temperature exposure. The results of the tests are reported in figure 3. Notwithstanding the slow heating rate set in the final stage of heating, the DSC system rearranged differently to guarantee isothermal conditions at 540°C. As a result, the heat flow in the first tenth of minutes of holding tine cannot be considered in terms of heat flow induced by microstructural variations. Similarly, the small heat flow changes with 3-5min frequency are correlated to small furnace power changes to guarantee isothermal conditions.
Nevertheless, different thermal events can be observed from the heat flow curves of the three alloys. A356 shows no evident exothermic peak. E3, on the other hand, is characterized by an exothermic peak at approximately 1.2 h and, finally, EZ35 by an exothermic peak at approximately the same time and another broader exothermic event from 2.5 to 4 h.

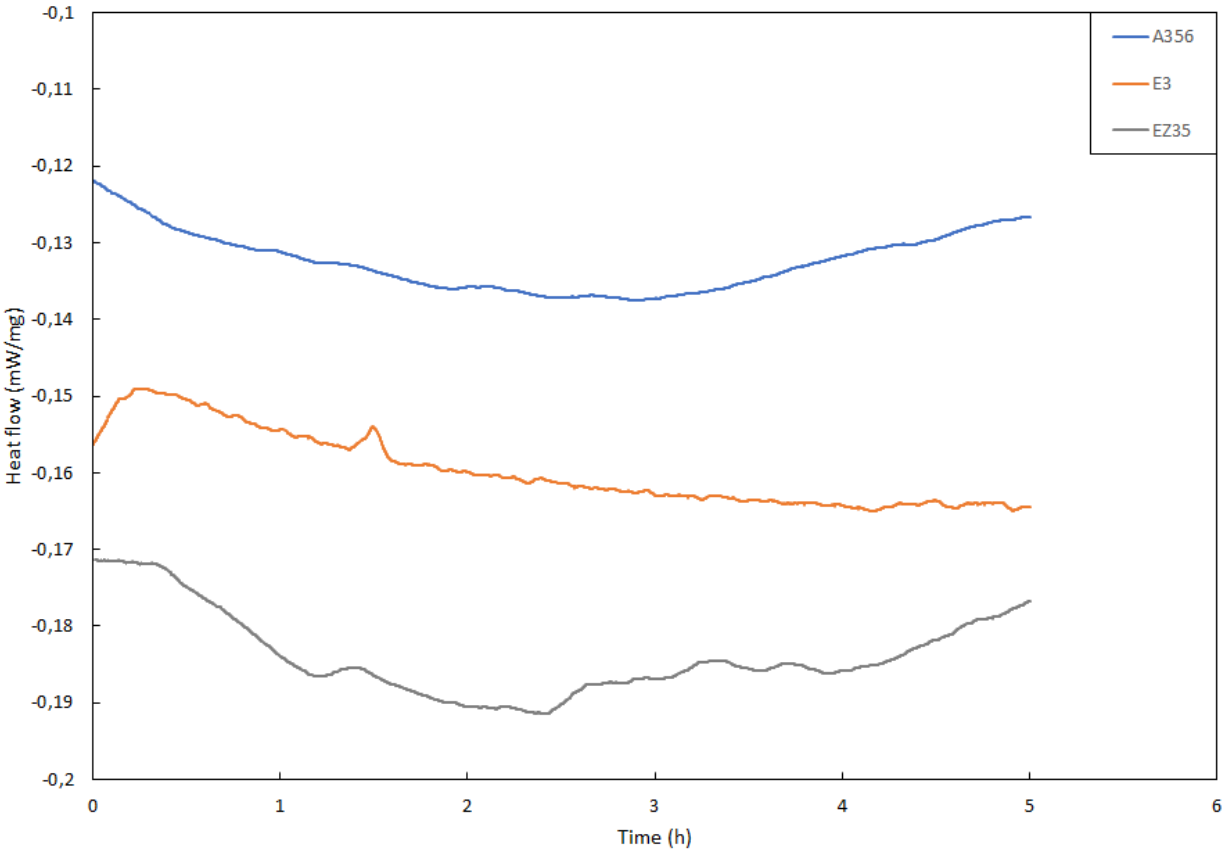


**Figure 3:** Isothermal DSC scans simulating SHT of the alloys.

*3.3 Microstructural characterization*

STEM micrographs of the studied alloys in the T6 state are reported in figure 4.

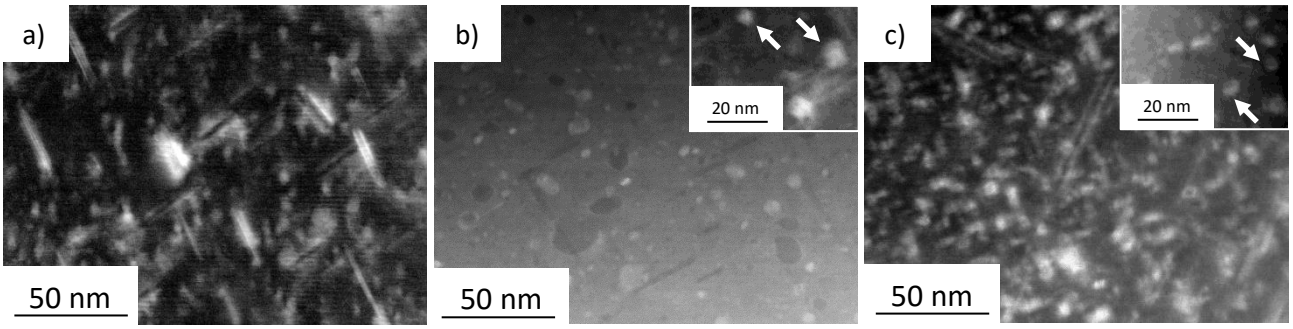


**Figure 4:** Representative Annular Dark Field (ADF) STEM micrographs in the T6 condition of a) A356, b) E3 and c) EZ35. Insert in figure c) highlights the presence of anti-phase boundaries in small intra-dendritic dispersoids. Micrographs are taken along the $<1\ 0\ 0>_{Al}$ crystallographic direction.

Figure 4a) shows that A356 is characterized by the presence of rod-like dispersoids oriented along the <1 0 0> direction, which can be identified as β'' ($Mg_5Si_6$) according to EDX measurements. The average length and thickness of β'' rods are calculated to be 34.9 ± 3.1 nm and 3.3 ± 0.9 nm, respectively.

Figure 4b) shows the microstructure of E3 in the T6 temper. Needle-like β'' dispersoids (with average length and thickness of 30.2 ± 2.4 nm and 2.5± 0.4 nm, respectively) are found together with smaller spheroidal particles with bimodal size distribution. Bigger particles are characterized by an average radius of approximately 9.6 ± 0.4 nm, while smaller dispersoids are characterized by a radius of 2.1 ± 0.1 nm. According to EDX measurements, they can be identified as ($Al_3Er$) dispersoids, since they show an Er:Al atomic ratio of 2.5.
Figure 4c) shows the microstructure of EZ35 in the T6 temper. As in E3, β'' needles (with average length and thickness of 28.8 ± 1.4 nm and 2.2 ± 0.5 nm respectively) are present together with smaller, spheroidal dispersoids with bimodal size distribution. Bigger dispersoids have a slightly prolate shape with an average length of 7.5 ± 0.2 nm, while smaller dispersoids have a radius of 1.7 ± 0.1 nm. The just mentioned dispersoids are identified as $Al_3$(Er, Zr) core shell particles by means of EDX analyses.
Representative Annular Dark Field (ADF) and High Angular Annular Dark Field (HAADF) STEM micrographs of A356 after 168 h aging at 200 °C are reported in figure 5.

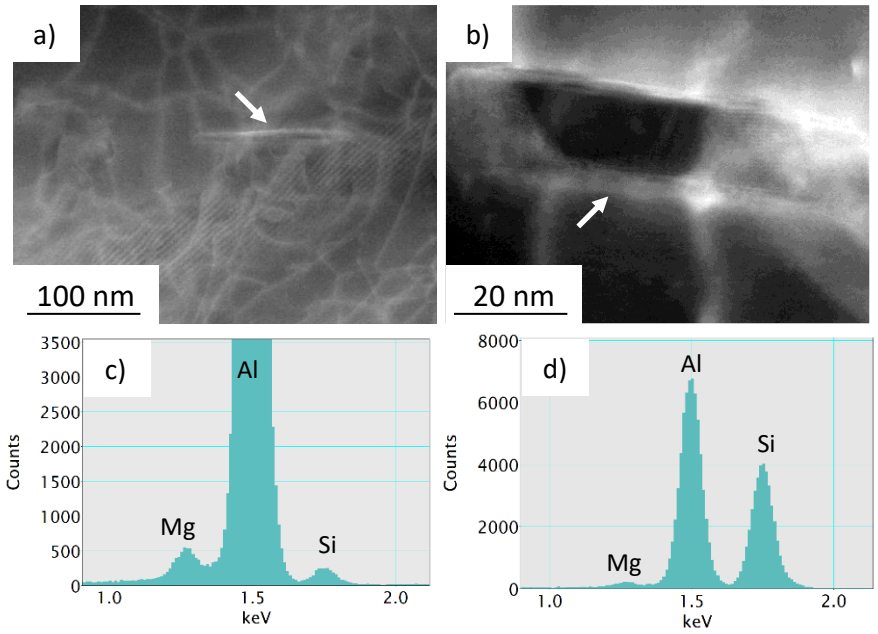


**Figure 5:** Representative ADF STEM micrographs showing intra-dendritic dispersoids in A356 after 168 h aging at 200 °C. a) reports a β' rod while b) shows a Si particle. c) and d) show the chemical composition of the dispersoids highlighted with arrows in a) and b), respectively.

Advanced stages of aging induce the precipitation of the typical dispersoids of excess Si Al-Mg-Si alloys, namely β' rod (a and c in figure 5) and Si dispersoids (b and d in figure 5).
The dispersoids present in intra-dendritic regions of E3 after 168 h aging at 200 °C are shown in figure 6. Particles similar to those observed in A356 are not documented in the above micrographs.

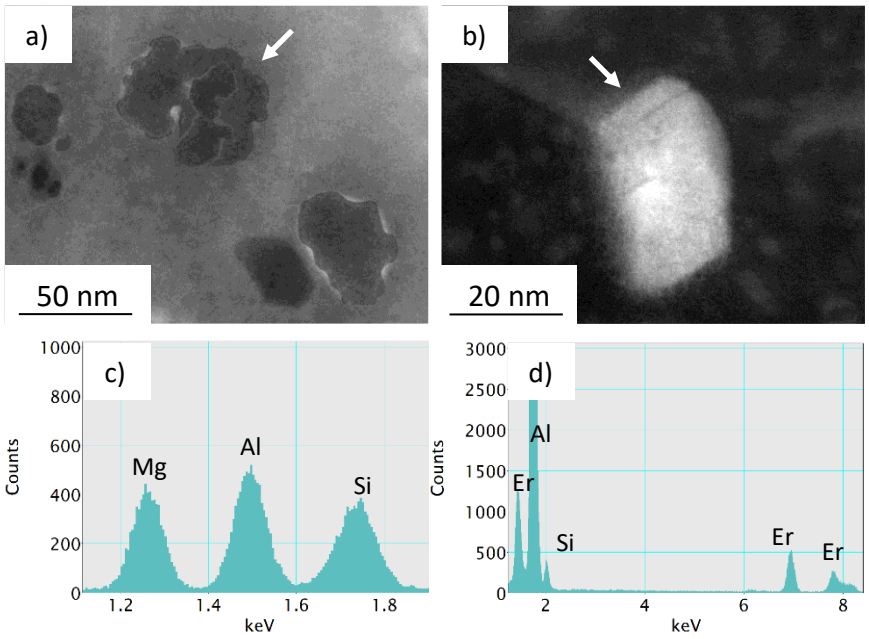


**Figure 6:** Representative ADF and HAADF (high angular annular dark field) STEM micrographs showing additional intra-dendritic dispersoids present in E3 after 168 h aging at 200 °C. a) U2 phase and b) Er containing dispersoid. c) and d) show the chemical composition of the dispersoids highlighted with arrows in a) and b), respectively.

From figure 6a) emerges that the addition of Er promotes the precipitation of complex-shaped dispersoids. The EDX spectrum reported in figure 6c), was used to quantify the chemical composition of the dispersoids ($Al_{1.3}Mg_{1.1}Si$). Together with Mg- and Si-containing dispersoids, particles Er-containing dispersoids (figures 6b and d) and Si-rich dispersoids, with a morphology and chemical composition equivalent to those visible in figure figures 5b) and d) are found in the alloy's microstructure.
Finally, the dispersoids in intra-dendritic regions of EZ35 in addition to those shown in figure 6 are reported in figure 7.

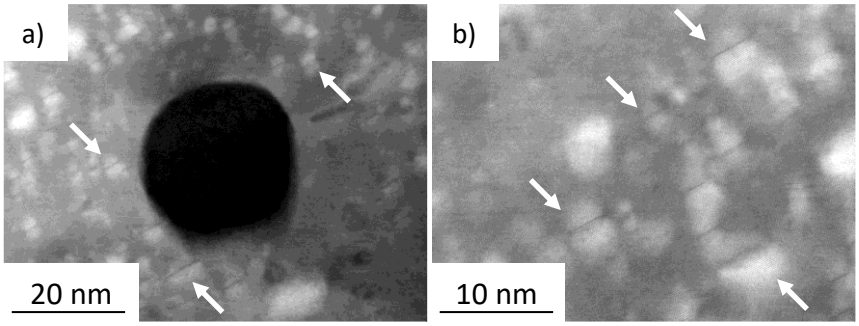


**Figure 7:** Representative ADF STEM micrographs showing intra-dendritic dispersoids present in EZ35 after 168 h aging at 200 °C. a) Si particle surrounded by small spheroidal dispersoids and b) higher magnification micrograph showing small spheroidal dispersoids.

As it is visible from figure 7, intra-dendritic regions in EZ35 are characterized by a high number of dispersoids with a bi-modal size distribution. Smaller spherical dispersoids with an average radius of

2.1 ± 0.2 nm and prolate ellipsoids with a major axis of 8.2 ± 0.2 nm. Both families of dispersoids are characterized by the presence of no-contrast lines of two to three atomic layers (similarly to Guinier Preston zones), oriented along the <1 0 0> directions.
STEM observations were also focused on characterizing the influence of Er and Zr additions on the morphology of eutectic Si particles. STEM micrographs of eutectic Si for E3 alloy are reported in Figure 8.

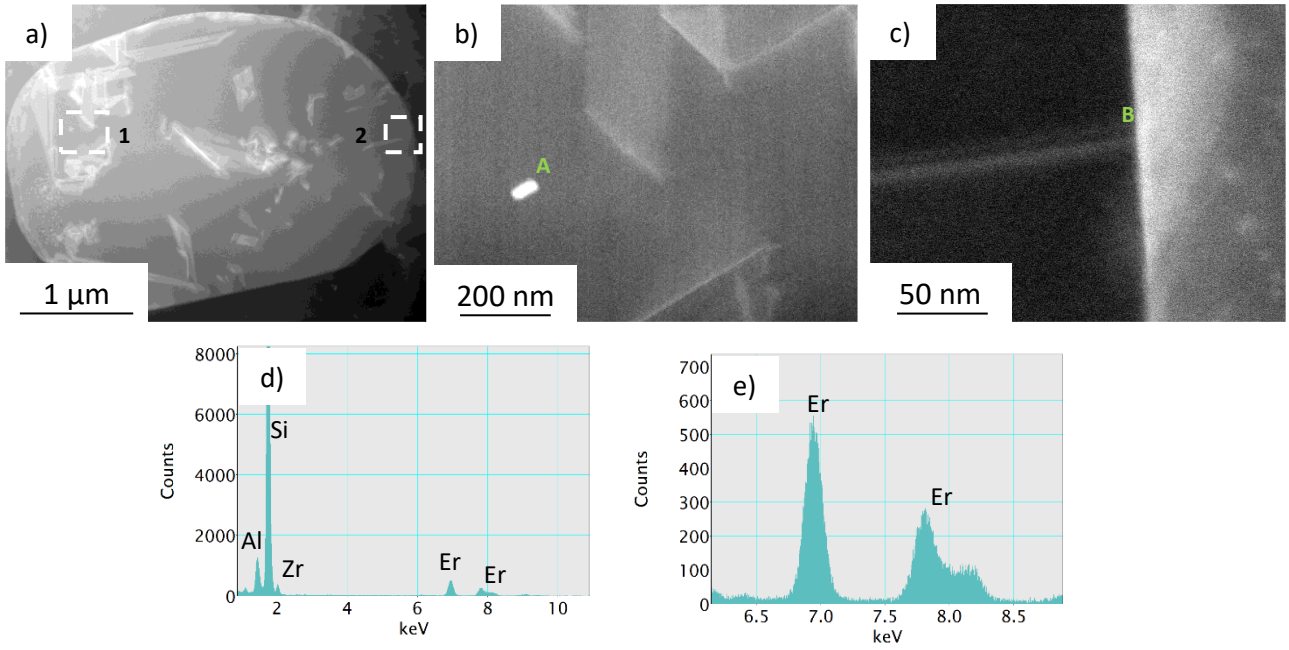


**Figure 8:** STEM micrographs of E3 showing a) eutectic Si particle, b) higher magnification micrograph of region 1 in a), c) higher magnification micrograph of region 2 in a), d) chemical composition of particle A and e) EDX spectrum showing the presence of Er at position B (interface between eutectic Si and Al).

As it is seen in figure 8a), eutectic Si is characterized by a high number of twins. Figure 8b) highlights the presence of Er-containing small particles in the inner regions of the eutectic (A in figure 8b and corresponding EDX spectrum in figure d). The presence of Zr in the EDX spectrum is most probably due to a contamination of the reference alloy.
EDX analysis performed at point B (at the Si-Al interface, as shown in figure 8c) and reported in figure 8e) shows that the Si-Al interface is enriched in Er; on the other hand, no Er atoms are found along Si twins nor Er-rich clusters are found at twins' intersection.
STEM micrographs of eutectic Si for EZ35 are reported in Figure 9.

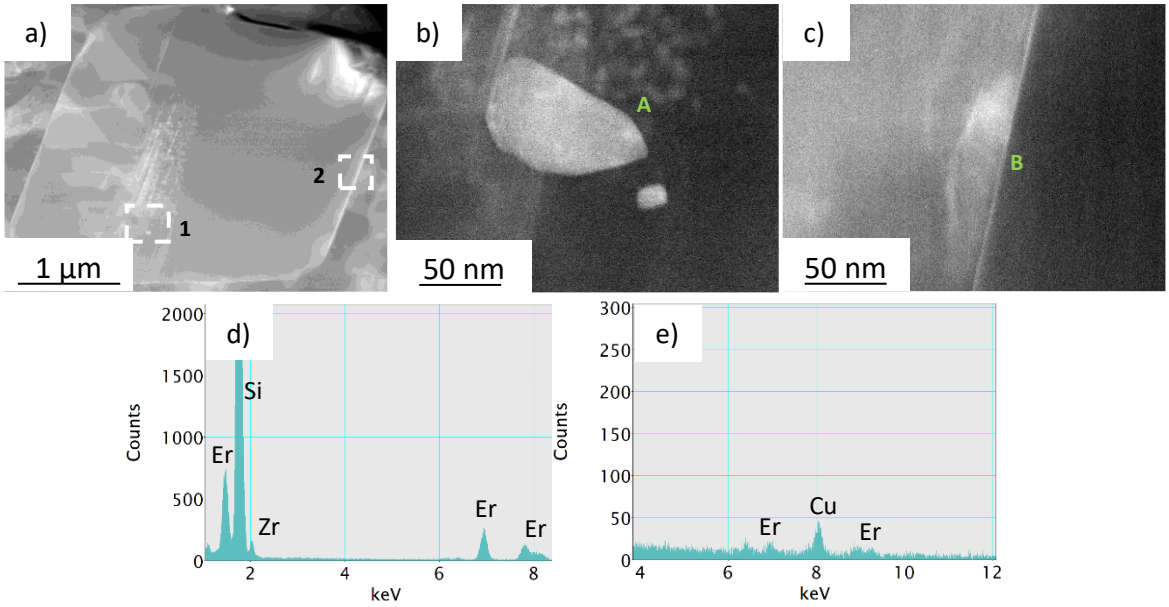


**Figure 9:** HAADF STEM micrographs of EZ35 showing a) eutectic Si particle, b) higher magnification micrograph of region 1 in a), c) higher magnification micrograph of region 2 in a), d) chemical composition of particle A and e) chemical composition at position B (interface between eutectic Si and Al). Cu peak is caused by the sample holder.

Like in E3, eutectic Si in EZ35 is characterized by the presence of twins, as shown in figure 9a). In figure 9b), the presence of small Er- and Zr-containing particles in the inner regions of eutectic Si is highlighted. The particles reported in figure 9b) have a chemical composition (figure 9d) which is similar to the one reported in figure 8d) for equivalent particles in alloy E3, with a slight Zr enrichment. Similarly, to what it is observed for E3 (figures 8c and 8e), the interface between eutectic Si and Al is enriched in Er, as visible from figures 9c) and 9e).

## 4. Discussion

The microhardness evolution of the solution treated A356 alloy, reported in figure 1, shows a monotonic decrease as a function of the SHT time, which is connected to the dissolution of intermetallic compounds. It is known from literature, in fact, that $Mg_2Si$ and $Al_8FeSi_6Mg_3$ precipitate forms during solidification and dissolve during high temperature exposure.

E3 displays a more complex microhardness trend. It shows a peak at approximately 0.5 h, after an initial microhardness drop. The hardness increase could be related to the formation of Er-containing dispersoids during SHT, namely $Al_3Er$, as found from STEM micrographs reported in figure 4b). Their formation is also suggested by the exothermic peak at slightly higher times in the isothermal DSC scans reported in figure 3. Since the conventional SHT time adopted in the present investigation is longer than that leading to peak hardness, it is reasonable that Er-containing particles coarsen above the critical radius for coherency loss. It is known from literature that the critical radius for coherency loss of $Al_3Er$ ranges from 8.0 to 9.1 nm [18], because of the relatively high lattice parameter mismatch between Al matrix and the dispersoids (+ 4.08%, as found in [19]). The radius for coherency loss is similar to the one measured for bigger spheroidal dispersoids shown in figure 4b).

Finally, the microhardness evolution of EZ35 is characterized by a first microhardness peak, similar to the one observed for E3 and connected to Er-rich dispersoids precipitation, and by a second increase at approximately 2 h followed by a plateau. The second microhardness increase can be related to the formation of a Zr-rich phase. The possibility that the Zr-phase formed on pre-existing

Er-rich dispersoids (as in dispersoids observed in [13-17]) as well as that they further evolved during SHT cannot be confirmed since STEM observations were carried out only on samples with 5h SHT. DSC scans show a first exothermic peak, connected to the precipitation of Er-rich dispersoids and a broad exothermic event occurring between 2 and 4 hours holding at 540°C. The microhardness of Er- and Zr-containing alloys after 5h SHT is higher with respect to the one of A356, further confirming that precipitation occurred during SHT.

Focusing the attention on the following aging behaviour, the part of aging curves up to the peak value (reported in figure 2 ) show a first steep increase in hardness, up to 1h, which could be connected to the precipitation of Mg-Si co-clusters (GP-II) promoted by the non-equilibrium quenched-in vacancies after SHT. GP-II are known to be fully coherent with the Al matrix, because of the high amount of Al [20]. As aging proceeds, Mg and Si diffuse to the GP-II dispersoids and continuously replace Al, leading to a gradual phase transition from GP-II to β'' [21]; this caused the reduction of the slope of the aging curves of alloys A356 and E3 after 1h aging visible in figure 2. The growth of β'' needles leads to the formation of elastic strain energy at the interface with the matrix, leading to the microhardness increase visible for A356 and E3 between 2 and 3 h.

STEM micrographs reported in figure 4 show the strengthening dispersoids present in the alloys' microstructure in the T6 temper. As it is shown in figure 4a), A356 is characterised by the presence of β'' needles, as it was described in several literature works [6, 22, 23]. Their size is in agreement with the one measured in other studies [6, 22, 23].

The microstructure of alloy E3 is characterized, in intra-dendritic regions, by β'' needles and a bimodal size distribution of small spheroidal dispersoids, which were identified as $Al_3Er$ (Figure 4b). β'' needles are characterized by a relatively lower size with respect to that measured in A356. The higher amount of intermetallic compounds containing Mg and Si in the microstructure of the alloy, which do not dissolve during thermal treatment [10], may reduce the concentration of Mg and Si in solid solution, contributing to the lower size of β'' needles.

It is reasonable to suppose that Precipitation of $Al_3Er$ dispersoids during aging accounts for the increased microhardness difference with respect to A356 as a function of aging time.

STEM observations of EZ35 in the T6 temper (Figure 4c) highlight also in this alloy the combined presence of β'' needles and of a bimodal size distribution of small spheroidal dispersoids in the intra-dendritic regions, identified as $Al_3$(Er, Zr). The even higher amount of primary intermetallic compounds containing Mg and Si in EZ35 with respect to E3 and A356 found in [24] may contribute, in addition to the shorter aging time to reach T6 temper, to the reduced size of β'' needles in the alloy. As for E3, it can be considered that bigger spheroidal $Al_3$(Er, Zr) dispersoids formed during SHT, while smaller dispersoids possibly precipitate during subsequent aging at 200 °C, accounting for the increased microhardness of the alloy. The lower size of spheroidal dispersoids formed in both heat treatment steps in EZ35 is possibly related to the reduced coarsening Zr-containing of particles [18, 25]. It is known, in fact, that the diffusion coefficient of Zr in Al is lower than that of the other alloying elements [18, 25].

After 168h aging at 200°C the three investigated alloys are clearly in overaged condition. The dispersoids present in the microstructure underwent several compositional and morphological changes with respect to T6 temper. The particles of βprecipitation sequence in the investigated overaged condition had already lost their coherency with the matrix. The loss of most of their strengthening effect is witnessed by the reduction in hardness

A356 is characterized by the presence of β' rods and Si dispersoids, as it is visible from figure 5a) and b), which are both characteristics of the advanced aging stages of Al-Mg-Si alloys with excess Si [23].

E3 is characterized by the presence of dispersoids with $Al_{1.3}Mg_{1.1}Si$ chemical composition instead of β' rods (figure 6a and c). The chemical composition of Mg- and Si-containing dispersoids is in good agreement with respect to the one that was given in literature for U2 (AlMgSi) [26, 27]; the preferential precipitation of U2 instead of β' is probably caused by the lower amount of Mg in solid solution after SHT, due to the presence of Mg-containing intermetallic compounds that are not

dissolved during thermal treatment, as it was demonstrated in [10]. As concerns $Al_3Er$ particles, they underwent coarsening during aging and they lost the coherency with the matrix, as it is shown in figure 6b). The coherency loss during aging contributed to the microhardness decrease observed in figure 2.
In EZ35 U2 dispersoids, with a very similar chemical composition and morphology of those in E3, and Si particles, with no significant difference with respect to those of the other alloys, formed after prolonged aging times. Differently to the other two alloys, the intra-dendritic regions of EZ35 are characterized by a high number of small, spheroidal dispersoids coherent with the matrix (as it is possible to see from the presence of a no-contrast zone in figure 7a). Higher magnification STEM micrographs highlighted more clearly the bimodal size distribution of spheroidal dispersoids, that is still present after 168 h aging. The average particles size slightly increased, passing from a major axis of 7.2 ± 0.2 nm in the T6 temper to 8.0 ± 0.2 nm in the overaged condition for the bigger dispersoids and from a radius of 1.7 ± 0.1 nm to a radius of 2.1 ± 0.2 nm for smaller dispersoids. The shape of the particles is not significantly affected by the exposure to the aging temperature, possibly due to the low diffusion coefficient of Zr in Al at the aging temperature. Further, it is known that the addition of Zr reduces the lattice misfit between the dispersoids and the matrix (from + 4.08% for $Al_3Er$ to + 0.75% for $Al_3(Er, Zr)$ [19]), consequently increasing the minimum radius for particles coherency loss. Literature studies, in fact, demonstrated that the radius for coherency loss of $Al_3(Er, Zr)$ is approximately 20 nm [19], which is much higher than the radius for coherency loss of $Al_3Er$ (8.0-9.1 nm [18]).
Alloys chemical composition also influenced eutectic Si. High magnification STEM micrographs in the inner regions of Si, reported in figure 8b), show the presence of Er-containing particles and a high number of twins (figure 8a). Literature studies performed on Al-Si alloys with the additions of modifying elements, like Sr and Eu, showed the presence of similar particles, which were identified as $Al_2Si_2X$, with X the modifying element [28, 29]. The particles inside eutectic Si showed in figure figure 8b) can thus be identified as $Al_2Si_2Er$. The possible identification of this phase is also supported by the isotherm section of the ternary Al-Si-Er phase diagram reported in [30]. STEM micrographs taken at the interface between Al and Si and relative EDX analyses (figure 8c and e, respectively) show that there is an enrichment in Er at the interface. The enrichment can be possibly explained considering the behaviour of modifying elements. It was shown, for example, that Sr and Na atoms adsorb along the $<1\ 1\ 2>_{Si}$ growth direction and at the twins' intersections, being responsible for impurity induced twinning and twin plane re-entrant edge poisoning [31]; assiming that Er atoms behave similarly, it is possible to consider that the high temperature exposure during thermal treatment stimulated a process of pipe diffusion of Er atoms along the twins shown in figure 8a), allowing solute accumulation at the Al-Si interface. No Er atom, in fact, is observed along Si twins or at twins' intersections. The high number of twins suggests the modifying effect of Er on eutectic Si.
A similar situation occurs in EZ35; eutectic Si is characterized by the presence of numerous twins (figure 9a); intermetallic compounds similar to those observed in figure 8b) are present also in Zr-containing alloy (figure 9b), but with a slight enrichment in Zr in the chemical composition (visible comparing figures 8d and 9d). These particles could be proposed as $Al_2Si_2(Er, Zr)$. An enrichment in Er is visible also at the interface between Al and Si in EZ35 (figures 9c and 9e), but no Zr peak emerges from EDX analyses, probably indicating that this element does not play a significant role in Si modification.

## 5. Conclusions

The scope of this paper was to study the influence of minor additions of Er and Zr on microstructural modification in Al7Si0.4Mg alloy during solution heat treatment and aging up to relatively long times. From the analyses of the obtained results it can be concluded that:

- Er and Zr additions induced the precipitation of dispersoids during solution heat treatment, as it was demonstrated by microhardness measurements of samples subjected to different SHT times and isothermal DSC scans at the solubilization temperature;
- High temperature thermal treatments promoted the formation of a Er-rich layer at the eutectic Si-Al interface;
- Aging up to the T6 temper induced the formation of additional small Er- and Zr-containing strengthening particles which were coherent with the matrix, explaining the higher microhardness of modified alloys;
- Er and Zr additions influenced the late stages of aging of A356 alloy, hindering the precipitation of β' rods, while promoting the formation of U2 dispersoids;
- Er- and Zr-containing strengthening particles slightly coarsened during aging, contributing to microhardness loss of the alloys;
- The intra-dendritic regions of EZ35 are characterized by a high number of small, coherent dispersoids that can justify the higher residual microhardness of the alloy after 168 h aging.

## 6. References


[1] L F Mondolfo, Metallography of Aluminum Alloys, John Wiley & Sons, Inc, London, 1943.
[2] R.X. Li, R. D. Li, Y. H. Zhao, L. Z. He, C. X. Li, H. R. Guan, Z. Q. Hu, Age-hardening behavior of cast Al–Si base alloy, Materials Letters, 58 (2004) 2096-2101.
[3] E. Sjölander, S. Seifeddine, The heat treatment of Al–Si–Cu–Mg casting alloys, Journal of Materials Processing Technology, 10 (2010) 1249-1259.
[4] Q. G. Wang, C. J. Davidson, Solidification and precipitation behaviour of Al-Si-Mg casting alloys, Journal of Materials Science, 36 (2001) 739-750.
[5] C. H. Caceres, C. J. Davidson, J. R. Griffiths, Q. G. Wang, The effect of Mg on the microstructure and mechanical behavior of Al-Si-Mg casting alloys, Metallurgical and Materials Transactions A, 30 (1999) 2611-2618).
[6] N. Chomsaeng, M. Haruta, T. Chairuangsri, H. Kurata, S. Isoda, M. Shiojiri, HRTEM and ADF-STEM of precipitates at peak-ageing in cast A356 aluminium alloy, Journal of Alloys and Compounds 496 (2010) 478–487.
[7] R. Vissers, M.A. van Huis, J. Jansen, H.W. Zandbergen, C.D. Marioara, S.J. Andersen, The crystal structure of the β' phase in Al–Mg–Si alloys, Acta Materialia 55 (2007) 3815–3823.
[8] Z.M. Shi, Q. Wang, G. Zhao, R. Y. Zhang, Effects of erbium modification on the microstructure and mechanical properties of A356 aluminum alloys, Materials Science and Engineering A, 626 (2015) 102-107.
[9] X. Hu, F. Jiang, F. Ai, H. Yan, Effects of rare earth Er additions on microstructure development and mechanical properties of die-cast ADC12 aluminum alloy, Journal of Alloys and Compounds, 538 (2012) 21-27.
[10] M. Colombo, E. Gariboldi, A. Morri, Er addition to Al-Si-Mg-based casting alloy: Effects on microstructure, room and high temperature mechanical properties, Journal of Alloys and Compounds, 708 (2017) 1234-1244.
[11] A. R. Farkoosh, X. G. Chen, M. Pekguleryuz, Dispersoid strengthening of a high temperature Al–Si–Cu–Mg alloy via Mo addition, Materials Science and Engineering A 620 (2015) 181–189.
[12] A. R. Farkoosh, X. G. Chen, M. Pekguleryuz, Interaction between molybdenum and manganese to form effective dispersoids in an Al–Si–Cu–Mg alloy and their influence on creep resistance, Materials Science and Engineering A 627 (2015) 127–138.
[13] H. Li, J. Bin, J. Liu, Z. Gao, X. Lu, Precipitation evolution and coarsening resistance at 400 °C of Al microalloyed with Zr and Er, Scripta Materialia, 67, 2012, 73-76.
[14] S.P. Wen, K.Y. Gao, Y. Li, H. Huang, Z.R. Nie, Synergetic effect of Er and Zr on the precipitation hardening of Al–Er–Zr alloy, Scripta Materialia, 65, 2011, 592-595.

[15] H. Li, Z. Gao, H. Yin, H. Jiang, X. Sua, J. Bina, Effects of Er and Zr additions on precipitation and recrystallization of pure aluminum, Scripta Materialia, 68, 2013, 59-62.
[16] S.P. Wen, K.Y. Gao, H. Huang, W. Wang, Z.R. Nie, Precipitation evolution in Al–Er–Zr alloys during aging at elevated temperature, Journal of Alloys and Compounds, 574, 2013, 92-97.
[17] Z. Gao, H. Li, Y. Lai, Y. Ou, D. Li, Effects of minor Zr and Er on microstructure and mechanical properties of pure aluminum, Materials Science and Engineering: A, 580, 2013, 92-98.
[18] Y. Zhang, K. Gao, S. Wen, H. Huang, Z. Nie, D. Zhou, The study on the coarsening process and precipitation strengthening of $Al_3Er$ precipitate in Al–Er binary alloy, Journal of Alloys and Compounds, 610 (2014) 27-34.
[19] S.P. Wen, K.Y. Gao, H. Huang, W. Wang, Z.R. Nie, Precipitation evolution in Al–Er–Zr alloys during aging at elevated temperature, Journal of Alloys and Compounds 574 (2013) 92–97.
[20] C. D. Marioara, S. J. Andersen, J. Jansen, H. W. Zandbergen, Atomic Model for GP-zones in a 6082 Al–Mg–Si system, Acta Materialia, 49 (2001) 321-328.
[21] C.D. Marioara, S.J. Andersen, J. Jansen, H.W. Zandbergen, The influence of temperature and storage time at RT on nucleation of the β'' phase in a 6082 Al–Mg–Si alloy, Acta Materialia 51 (2003) 789–796.
[22] A. Gaber, N. Afify, M.S. Mostafa, G. Abbady, Effect of heat treatment on the precipitation in Al–1 at.% Mg–x at.% Si (x = 0.6, 1.0 and 1.6) alloys, Journal of Alloys and Compounds 477 (2009) 295–300.
[23] A.K. Gupta, D.J. Lloyd, S.A. Court, Precipitation hardening processes in an Al–0.4%Mg–1.3%Si–0.25%Fe aluminum alloy, Materials Science and Engineering A301 (2001) 140–146.
[24] M. Colombo, E. Gariboldi, A. Morri, Influences of different Zr additions on the microstructure, room and high temperature mechanical properties of an Al-7Si-0.4Mg alloy modified with 0.25%Er, Materials Science and Engineering A, 713 (2018) 151-160.
[25] K. Hirano, S. Fujikawa, Impurity diffusion in Aluminum, Journal of Nuclear Materials 69 & 70 (1978) 564-566.
[26] M.A. van Huis, J.H. Chen, H.W. Zandbergen, M.H.F. Sluiter, Phase stability and structural relations of nanometer-sized, matrix-embedded precipitate phases in Al–Mg–Si alloys in the late stages of evolution, Acta Materialia 54 (2006) 2945–2955.
[27] S.J. Andersen, C.D. Marioara, A. Frøseth, R. Vissers, H.W. Zandbergen, Crystal structure of the orthorhombic U2-$Al_4Mg_4Si_4$ precipitate in the Al–Mg–Si alloy system and its relation to the β' and β'' phases, Materials Science and Engineering A 390 (2005) 127–138.
[28] J. H. Li, X. D. Wang, T. H. Ludwig, Y. Tsunekawa, L. Arnberg, J. Z. Jiang, P. Schumacher, Modification of eutectic Si in Al–Si alloys with Eu addition, Acta Materialia, (2015) 153-163.
[29] P. Srirangam, S. Chattopadhyay, A. Bhattacharya, S. Nag, J. Kaduk, S. Shankar, R. Banerjee, T. Shibata, Probing the local atomic structure of Sr-modified Al–Si alloys, Acta Materialia, 65 (2014) 185-193.
[30] V. Raghavan, Al-Er-Si (Aluminum-Erbium-Silicon), Journal of Phase Equilibria and Diffusion, 31 (2010) 44-45.
[31] J.H. Li, M. Albu, F. Hofer, P. Schumacher, Solute adsorption and entrapment during eutectic Si growth in A–Si-based alloys, Acta Materialia 83 (2015) 187–202.